Intrinsic Electronic Conduction Mechanisms in Self-Assembled Monolayers

Wenyong Wang, Takhee Lee, and Mark A. Reed

Departments of Electrical Engineering, Applied Physics, and Physics, Yale University, P.O. Box 208284, New Haven, CT 06520, USA

Summary. A review on the mechanisms and characterization methods of molecular electronic transport is presented. Using self-assembled monolayers (SAMs) of alkanethiols in a nanometer scale device structure, tunneling is unambiguously demonstrated as the main conduction mechanism for large bandgap SAMs, exhibiting well-known temperature and length dependencies. Inelastic electron tunneling spectroscopy exhibits clear vibrational modes of the molecules in the device, presenting the first direct evidence of the presence of molecules in a molecular device.

1 Introduction

The suggestion [1] and demonstration [2] of utilizing molecules as the active region of electronic devices has recently generated considerable interest in both the basic transport physics and potential technological applications of molecular electronics [3],[4]. However some reports of molecular mechanisms in electronic devices [5],[6] have been shown to be premature and due to filamentary conduction [7], highlighting the fabrication sensitivity of molecular structures and the need to institute reliable controls and methods to validate true molecular transport [8]. A related problem is the characterization of molecules in the active device structure, including their configuration, bonding, and indeed even their very presence. Here we present results on well-understood molecular assemblies, which exhibit an understood classical transport behavior, and which can be used as a control for eliminating (or understanding) fabrication variables. Utilizing tunneling spectroscopic methods, we present the first unambiguous evidence of the presence of molecules in the junction.

A molecular system whose structure and configuration are sufficiently well-characterized such that it can serve as a standard is the extensively studied alkanethiol ($CH_3(CH)_{n-1}SH$) self-assembled monolayer (SAM) [9]. This system is useful as a control since properly prepared SAMs form single van der Waals crystals [9],[10], and presents a simple classical metal-insulator-metal (M-I-M) tunnel junction when fabricated between metallic contacts due to the large HOMO-LUMO gap (HOMO: highest occupied molecular orbital, LUMO: lowest unoccupied molecular orbital) of approximately 8 eV [11],[12].

Various surface analytical tools have been utilized to investigate the surface and bulk properties of the alkanethiol SAMs, such as X-ray photoelectron spectroscopy [13], Fourier transform infrared spectroscopy (FTIR) [14], Raman spectroscopy [15], scanning tunneling microscopy (STM) [10], etc. Studies have shown that the bonding of the thiolate group to the gold surface is strong with a bonding energy of $\sim$ 1.7 eV [9]. STM topography examinations revealed that alkanethiols adopt the commensurate crystalline lattice characterized by a c(4×2) superlattice of a $(\sqrt{3} \times \sqrt{3})$R30° [10],[16]. FTIR investigation showed that the orientation of the alkanethiol SAMs on Au(111) surfaces are tilted $\sim 30°$ from the surface normal [17].

Electronic transport through alkanethiol SAMs have also been characterized by STM [18],[19], conducting atomic force microscopy [20]-[23], mercury-drop junctions [24]-[27], cross-wire junctions [28], and electrochemical methods [29]-[31]. These investigations are exclusively at ambient temperature clearly useful but insufficient for an unambiguous claim that the transport mechanism is tunneling (of course expected, assuming that the Fermi levels of the contacts lie within the large HOMO-LUMO gap). However in the absence of temperature-dependent current-voltage (I(V,T)) characteristics, other conduction mechanisms (such as thermionic, hopping, or filamentary conduction) can contribute and complicate the analysis, and thus such a claim is premature.

Utilizing a nanometer scale device structure that incorporates alkanethiol SAMs, we demonstrate devices that allow I(V,T) and structure-dependent measurements [32],[33] with results that can be compared with accepted theoretical models of M-I-M tunneling. The use of this fabrication approach is not special in any way (other than that we have so far found it to be successful) indeed we stress that any successful device fabrication method should yield the results described below if one is characterizing the intrinsic molecular transport properties.

The electronic transport is further investigated with the technique of inelastic electron tunneling spectroscopy (IETS) [33]. IETS was developed in the 1960s as a powerful spectroscopic tool to study the vibrational spectrum of organic molecules confined inside metal-oxide-metal junctions [34]-[38]. In our study IETS is utilized for the purpose of molecule identification, chemical bonding, and conduction mechanism investigation of the control SAMs. The exclusive presence of well-known vibrational modes of the alkanes used are direct evidence of the molecules in the device structure, something that has to date only been inferred (with good reason, but nonetheless not unambiguously). The vibrational modes, exclusively identified as alkanes (as well as contact modes) are difficult to interpret in any other way other than as components in the active region of the device. The specific spectral lines also yield intrinsic linewidths that may give insight into molecular conformation, and may prove to be a powerful tool in future molecular device characterization.

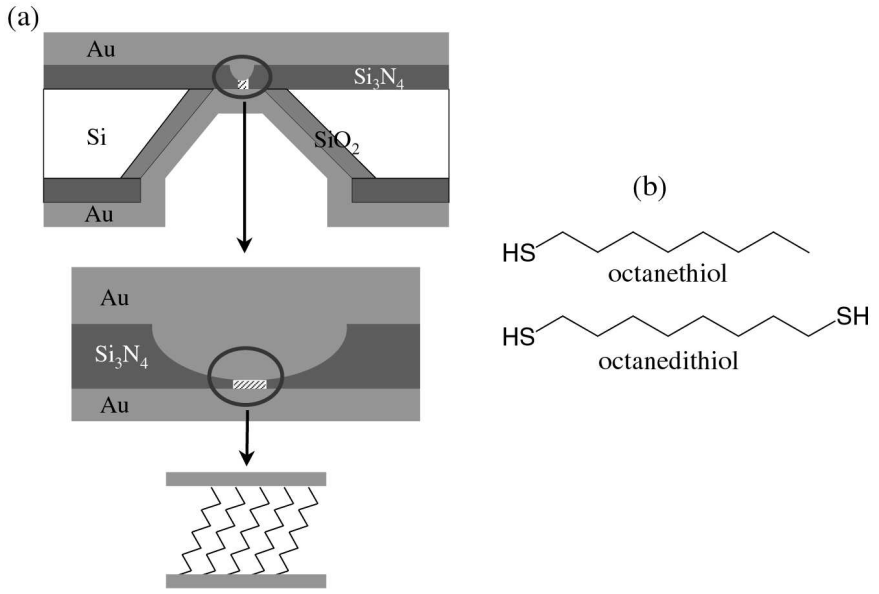

Fig. 1. Schematics of a nanometer scale device used in this study. (a) Top schematic is the cross section of a silicon wafer with a nanometer scale pore etched through a suspended silicon nitride membrane. Middle and bottom schematics show a Au/SAM/Au junction formed in the pore area. (b) The structures of octanethiol and octanedithiol are shown as examples

2 Experiment

Electronic transport measurements on alkanethiol SAMs were performed using a device structure similar to one reported previously [32],[33],[39]-[41]. In this device, as illustrated in Fig. 1(a), a number of molecules ($\sim$ several thousands) are sandwiched between two metallic contacts. This technique provides a stable device structure and makes cryogenic measurements possible. The device fabrication starts with a high resistivity silicon wafer with low stress Si_3N_4 film deposited on both sides by low pressure chemical vapor deposition (LPCVD). By standard photolithography processing, a suspended Si_3N_4 membrane (size of 40 μm $\times$ 40 μm and thickness of $\sim$ 70 nm) is fabricated on the topside of the wafer. Subsequent e-beam lithography and reactive ion etching creates a single pore with a diameter of tens of nanometers through the membrane. As the next step, 150 nm gold is thermally evaporated onto the topside of the wafer to fill the pore and form one of the metallic contacts.

The device is then transferred into a molecular solution to deposit the SAM layer. For our experiments, a $\sim$ 5 mM alkanethiol solution is prepared by adding $\sim$ 10 μL alkanethiols into 10 mL ethanol. The deposition is done in solution for 24 hours inside a nitrogen filled glove box with an oxygen level

of less than 100 ppm. Three alkanemonothiol molecules of different molecular lengthsoctanethiol [$CH_3(CH_2)_7SH$; denoted as C8, for the number of alkyl units], dodecanethiol [$CH_3(CH_2)_{11}SH$, denoted as C12], and hexadecanethiol [$CH_3(CH_2)_{15}SH$, denoted as C16] and one alkanedithiol moleculeoctanedithiol [$HS(CH_2)_8SH$, denoted as C8-dithiol] were used to form the active molecular components. As representative examples, the chemical structures of octanethiol and octanedithiol are shown in Fig. 1(b).

In order to statistically determine the pore size, test patterns (arrays

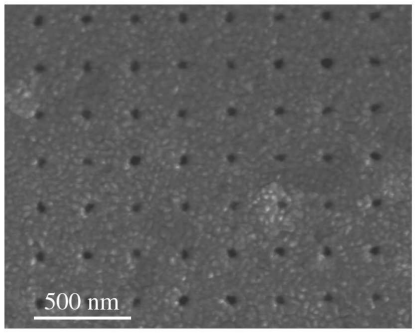

Fig. 2. A scanning electron microscope image of a representative array of pores used to calibrate device size. The scale bar is 500 nm

of pores) were created under similar fabrication conditions. Figure 2 shows a scanning electron microscope (SEM) image of such test pattern arrays. This indirect measurement of device size is done since SEM examination of the actual device can cause hydrocarbon contamination of the device and subsequent contamination of the monolayer. From regression analysis of 298 pores, the device sizes of the C8, C12, C16, and C8-dithiol samples are 50 $\pm$ 8, 45 $\pm$ 2, 45 $\pm$ 2, and 51 $\pm$ 5 nm in diameters, respectively. A more ideal (less parasitics) C8 sample supersedes that of previous reports [32], and derived parameters from the two data sets agree to within a standard error. We will use these device areas as the effective contact areas. Although one could postulate that the actual area of metal that contacts the molecules may be different, there is little reason to propose it would be different as a function of length over the range of alkanethiols used, and at most would be a constant systematic error. Further on we will show that the results from the current density agree with the results from length dependence, giving an independent check that the effective area is in fact the actual area.

The sample is then transferred in ambient conditions to an evaporator that has a cooling stage to deposit the opposing Au contact. During the thermal evaporation (under the pressure of 10^{-8} Torr), liquid nitrogen is kept flowing through the cooling stage in order to avoid thermal damage to the molecular layer [32],[42]. This technique reduces the kinetic energy of

evaporated Au atoms at the surface of the monolayer, thus preventing Au atoms from punching through the monolayer. For the same reason the evaporation rate is kept very low. For the first 10 nm gold evaporated, the rate is less than 0.1 Å/s. Then the rate is increased slowly to 0.5 Å/s for the rest of the evaporation and a total of 200 nm gold is deposited to form the contact.

The device is subsequently packaged and loaded into a low temperature cryostat. The sample temperature is varied from 300 to 4.2 K by flowing cryogen vapor onto the sample (and thermometer) using a closed loop temperature controller. Two-terminal dc I(V) measurements are performed using a semiconductor parameter analyzer. Inelastic electron tunneling spectra are obtained via a standard lock-in second harmonic measurement technique [34],[35]. A synthesized function generator is used to provide both the modulation and the lock-in reference signal. The second harmonic signal (proportional to d^2I/dV^2) is directly measured using a lock-in amplifier, which is checked to be consistent with a numerical derivative of the first harmonic signal (proportional to dI/dV). Various modulation amplitudes and frequencies are utilized to obtain the spectra. The ac modulation is added to a dc bias using operational amplifier-based custom circuitry [43].

3 Theoretical Basis

3.1 Possible Conduction Mechanisms

In Table 1, possible conduction mechanisms are listed with their characteristic current, temperature- and voltage-dependencies [44] (We do not discuss filamentary tunneling mechanisms, which are easier to categorize [45]. Based on whether thermal activation is involved, the conduction mechanisms fall into two distinct categories: (i) thermionic or hopping conduction which has temperature-dependent I(V) behavior and (ii) direct tunneling or Fowler-Nordheim tunneling which does not have temperature-dependent I(V) behavior. For example, thermionic and hopping conductions have been observed for 4-thioacetylbiphenyl SAMs [39] and 1,4-phenelyene diisocyanide SAMs [40]. On the other hand, the conduction mechanism is expected to be tunneling when the Fermi levels of contacts lie within the large HOMO-LOMO gap for short length molecule, as for the case of alkanethiol molecular system [11],[12]. Previous work on Langmuir-Blodgett alkane monolayers [46] exhibited a significant impurity-dominated transport component, complicating the analysis. I(V) measurements on self-assembled alkanethiol monolayers have also been reported [18]-[28],[47]; however all of these measurements were performed at fixed temperature (300 K) which is insufficient to prove tunneling as the dominant mechanism.

Table 1. Possible conduction mechanisms. Adapted from [44]

Conduction mechanism	Characteristic behavior	Temperature dependence	Voltage dependence
Direct tunneling*	$J \propto V \exp\left(-\frac{2d}{\hbar}\sqrt{2m\Phi}\right)$	none	$J \propto V$
Folwer-Lordheim tunneling	$J \propto V^2 \exp\left(-\frac{4d\sqrt{2m}\,\Phi^{3/2}}{3q\hbar V}\right)$	none	$\ln(J/V^2) \propto 1/V$
Thermionic emission	$J \propto T^2 \exp\left(-\frac{\Phi - q\sqrt{qV/4\pi\varepsilon d}}{kT}\right)$	$\ln(J/T^2) \propto 1/T$	$\ln(J) \propto V^{1/2}$
Hopping conduction	$J \propto V \exp\left(-\frac{\Phi}{kT}\right)$	$\ln(J/V) \propto 1/T$	$J \propto V$

* This characteristic of direct tunneling is valid for the low bias regime [see (3)].

3.2 Tunneling Models

To describe the transport through a molecular system having HOMO and LUMO energy levels, one of the applicable models is the Franz two-band model [48]-[51]. This model provides a non-parabolic energy-momentum E(k) dispersion relationship by considering the contributions of both the HOMO and LUMO energy levels [48]:

$$k^2 = \frac{2m^*}{\hbar^2} E \left(1 + \frac{E}{E_g}\right) \tag{1}$$

where k is the imaginary part of wave vector of electrons, m* is the electron effective mass, h ($= 2\pi\hbar$) is Planck's constant, E is the electron energy, and E_g is the HOMO-LUMO energy gap. From this non-parabolic E(k) relationship, the effective mass of the electron tunneling through the SAM can be deduced by knowing the barrier height of the metal-SAM-metal junction.

When the Fermi level of the metal is aligned close enough to one energy level (either HOMO or LUMO), the effect of the other distant energy level on the tunneling transport is negligible, and the widely used Simmons model [52] is an excellent approximation [53]. Simmons model expressed the tunneling current density through a barrier in the tunneling regime of $V < \Phi_B/e$ as [24],[52]

$$J = \frac{e}{4\pi^2\hbar d^2}\left\{\left(\Phi_B - \frac{eV}{2}\right) \times \exp\left[-\frac{2(2m)^{1/2}}{\hbar}\alpha\left(\Phi_B - \frac{eV}{2}\right)d\right]\right.$$
$$\left. - \left(\Phi_B + \frac{eV}{2}\right) \times \exp\left[-\frac{2(2m)^{1/2}}{\hbar}\alpha\left(\Phi_B + \frac{eV}{2}\right)d\right]\right\} \tag{2}$$

where m is the electron mass, d is the barrier width, Φ_B is the barrier height, and V is the applied bias. For molecular systems, the Simmons model has been modified with a parameter α [24],[32]. α is a unitless adjustable parameter that is introduced to provide either a way of applying the tunneling model of a rectangular barrier to tunneling through a nonrectangular barrier [24], or an adjustment to account for the effective mass (m*) of the tunneling electrons through a rectangular barrier [24],[32],[51],[54], or both. $\alpha = 1$ corresponds to the case for a rectangular barrier and bare electron mass. By fitting individual I(V) data using (2), Φ_B and α values can be obtained.

Equation (1) can be approximated in two limits: low bias and high bias as compared with the barrier height Φ_B. For the low bias range, (2) can be approximated as [52]

$$J \approx \left(\frac{(2m\Phi_B)^{1/2}e^2\alpha}{\hbar^2 d}\right) V exp\left[-\frac{2(2m)^{1/2}}{\hbar}\alpha(\Phi_B)^{1/2}d\right] \tag{3}$$

To determine the high bias limit, we compare the relative magnitudes of the first and second exponential terms in (2). At high bias, the first term is dominant and thus the current density can be approximated as

$$J \approx \left(\frac{e}{4\pi^2\hbar d^2}\right)\left\{\left(\Phi_B - \frac{eV}{2}\right) \times exp\left[-\frac{2(2m)^{1/2}}{\hbar}\alpha\left(\Phi_B - \frac{eV}{2}\right)d\right]\right\} \tag{4}$$

The tunneling currents in both bias regimes are exponentially dependent on the barrier width d. In the low bias regime the tunneling current density is $J \propto \frac{1}{d} exp(-\beta_0 d)$, where $\beta_0$is bias-independent decay coefficient:

$$\beta_0 = \frac{2(2m)^{1/2}}{\hbar}\alpha(\Phi_B)^{1/2} \tag{5}$$

while in the high bias regime, $J \propto \frac{1}{d^2} exp(-\beta_V d)$, where β_V is bias-dependent decay coefficient:

$$\beta_V = \frac{2(2m)^{1/2}}{\hbar}\alpha\left(\Phi_B - \frac{eV}{2}\right)^{1/2} = \beta_0\left(1 - \frac{eV}{2\Phi_B}\right)^{1/2} \tag{6}$$

At high bias β_V decreases as bias increases, which results from barrier lowering effect due to the applied bias.

4 Results

4.1 Current-Voltage Characteristics

Temperature-Variable Current-Voltage (I(V,T)) Measurement

In order to determine the conduction mechanism of self-assembled alkanethiol molecular systems I(V) measurements in a sufficiently wide temperature

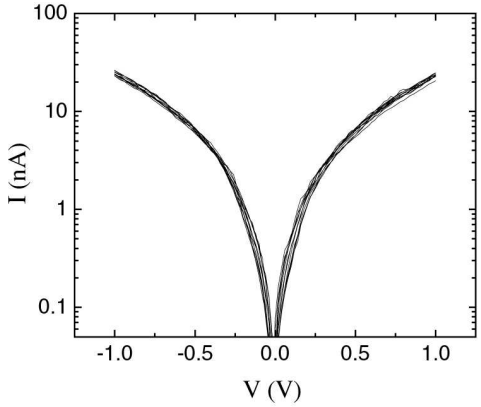

Fig. 3. Temperature-dependent I(V) characteristics of dodecanethiol (C12). I(V) data at temperatures from 300 to 80 K with 20 K steps are plotted on a log scale

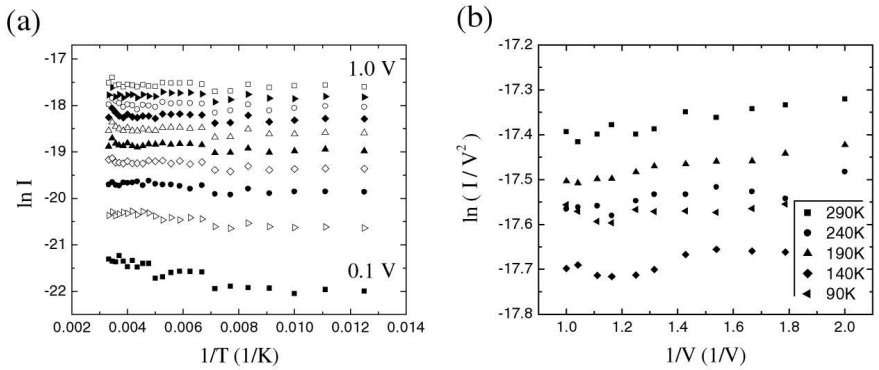

Fig. 4. (a) Arrhenius plot generated from the I(V) data in Fig. 3, at voltages from 0.1 to 1.0 Volt with 0.1 Volt steps. (b) Plot of ln(I^2/V) versus 1/V at selected temperatures

range (300 to 80 K) and resolution (10 K) were performed. Fig. 3 shows a representative I(V,T) characteristic of dodecanethiol (C12) measured with the device structure as shown in Fig. 1(a). Positive bias corresponds to electrons injected from the physisorbed Au contact [bottom contact in Fig. 1(a)] into the molecules. By using the contact area of 45 ± 2 nm in diameter determined from SEM study, a current density of 1,500 ± 200 A/cm^2 at 1.0 Volt is determined. No significant temperature dependence of the characteristics (from V = 0 to 1.0 Volt) is observed over the range from 300 to 80 K. An Arrhenius plot (ln(I) versus 1/T) of this is shown in Fig. 4(a), exhibiting little temperature dependence in the slopes of ln(I) versus 1/T at different bias and thus indicating the absence of thermal activation. There-

fore, we conclude that the conduction mechanism through alkanethiol is tunneling contingent on demonstrating a correct molecular length dependence. The tunneling through alkanethiol SAMs has been assumed as "through-bond" tunneling, i.e., along the tilted molecular chains between the metal contacts [21],[22],[31],[55]. Based on the applied bias as compared with the barrier height (Φ_B), the tunneling through a SAM layer can be categorized into either direct ($V < \Phi_B/e$) or Fowler-Nordheim ($V > \Phi_B/e$) tunneling. These two tunneling mechanisms can be distinguished due to their distinct voltage dependencies (see Table 1). Analysis of $\ln(I^2/V)$ versus $1/V$ [in Fig. 4(b)] shows no significant voltage dependence, indicating no obvious Fowler-Nordheim transport behavior in this bias range (0 to 1.0 Volt) and thus determining that the barrier height is larger than the applied bias, i.e., $\Phi_B >$ 1.0 eV. This study is restricted to applied biases $\leq$ 1.0 Volt and the transition from direct to Fowler-Nordheim tunneling requires higher bias. Having established tunneling as the conduction mechanism, we can now obtain the barrier height by comparing our experimental I(V) data with theoretical calculations from the aforementioned tunneling models.

Tunneling Characteristics through Alkanethiols

From the modified Simmons model [see (2)] by adjusting two parameters Φ_B and α, a nonlinear least squares fitting can be performed to fit the measured C12 I(V) data (calculation assuming $\alpha = 1$ has been previously shown not to fit I(V) data well for some alkanethiol measurements at fixed temperature (300 K)) [24]. By using a device size of 45 nm in diameter, the best fitting parameters (minimizing χ^2) for the room temperature C12 I(V) data were found to be $\Phi_B = 1.42 \pm 0.04$ eV and $\alpha = 0.65 \pm 0.01$, where the error ranges of Φ_B and α are dominated by potential device size fluctuations of 2 nm. Likewise, data sets were obtained and fittings were done for octanethiol (C8) and hexadecanethiol (C16), which yielded values $\{\Phi_B = 1.83 \pm 0.10$ eV and $\alpha = 0.61 \pm 0.01\}$ and $\{\Phi_B = 1.40 \pm 0.03$ eV, $\alpha = 0.68 \pm 0.01\}$, respectively.

Using $\Phi_B = 1.42$ eV and $\alpha = 0.65$, a calculated I(V) for C12 is plotted as a solid curve on a linear scale [Fig. (5a)] and a semi-log scale [Fig. (5b)]. A calculated I(V) for $\alpha = 1$ and $\Phi_B = 0.65$ eV (which gives the best fit at low bias range) is shown as the dashed curve in the same figure, illustrating that with $\alpha = 1$ only limited regions of the I(V) can be fit (specifically here, for V < 0.3 Volt). For the case of a rectangular barrier, the parameter fit presented above corresponds to an effective mass m* ($= \alpha^2$ m) of 0.42 m. In order to investigate the dependency of the Simmons model fitting on Φ_B and α, a fitting minimization analysis was undertaken on the individual Φ_B and α values as well as their product form of $\alpha\Phi_B^{1/2}$ in (5). $\Delta(\Phi_B, \alpha) = (\Sigma|I_{exp,V} - I_{cal,V}|^2)^{1/2}$ was calculated and plotted where $I_{exp,V}$ is the experimental current-voltage values and $I_{cal,V}$ is calculated using (2). 7,500 different $\{\Phi_B, \alpha\}$ pairs were used in the fittings with Φ_B ranging from

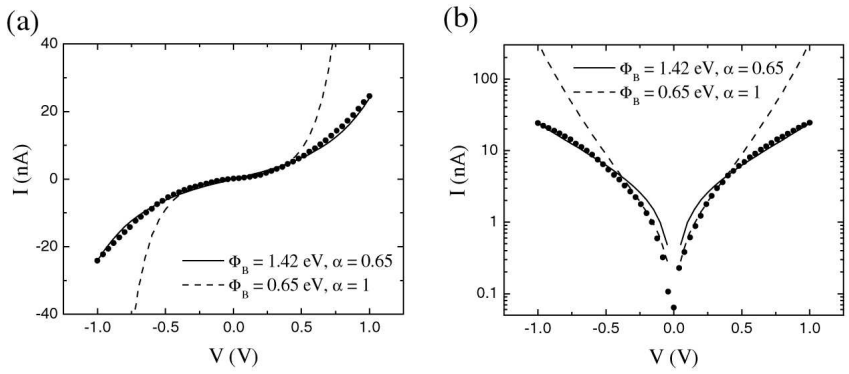

Fig. 5. Measured C12 I(V) data (circular symbols) is compared with calculation (solid curve) using the optimum fitting parameters of $\Phi_B = 1.42$ eV and $\alpha = 0.65$. The calculated I(V) from a simple rectangular model ($\alpha = 1$) with $\Phi_B = 0.65$ eV is also shown as the dashed curve. Current is plotted (a) on linear scale and (b) on log scale

1.0 to 2.5 eV (0.01 eV increment) and α from 0.5 to 1.0 (0.01 increment). Figure 6(a) is a representative contour plot of $\Delta(\Phi_B, \alpha)$ versus Φ_B and α values generated for the C12 I(V) data where darker regions correspond to smaller $\Delta(\Phi_B, \alpha)$ and various shades represent half order of magnitude $\Delta(\Phi_B, \alpha)$ steps. The darker regions represent better fits of (1) to the measured I(V) data. In the inset in Fig. 6(a) one can see there is a range of possible Φ_B and α values yielding minimum fitting parameters. Although the tunneling parameters determined from the previous Simmons tunneling fitting $\{\Phi_B = 1.42$ eV and $\alpha = 0.65\}$ lie within this minimum region in this figure, there is a distribution of other possible values.

A plot of $\Delta(\Phi_B, \alpha)$ versus $\alpha\Phi_B^{1/2}$ for the same device reveals a more pronounced dependence, and is shown in Fig. 6(b). This plot indicates the fitting to the Simmons model sharply depends on the product of $\alpha\Phi_B^{1/2}$. For this plot the $\Delta(\Phi_B, \alpha)$ is minimized at $\alpha\Phi_B^{1/2}$ of 0.77 $(\text{eV})^{1/2}$ corresponding to a β_0 value of 0.79 Å^{-1} from (5). The C8 and C16 devices showed similar results, indicating the Simmons tunneling model has a strong $\alpha\Phi_B^{1/2}$ dependence.

Length-Dependent Tunneling through Alkanethiols

Three alkanethiols of different molecular length, C8, C12, and C16 were investigated to study length-dependent tunneling behavior. Figure 7 is a semi-log plot of tunneling current densities multiplied by molecular length (Jd at low bias and Jd^2 at high bias) as a function of the molecular length for these alkanethiols. The molecular lengths used in this plot are 13.3, 18.2, and 23.2 Å for C8, C12, and C16, respectively (each molecular length was determined by

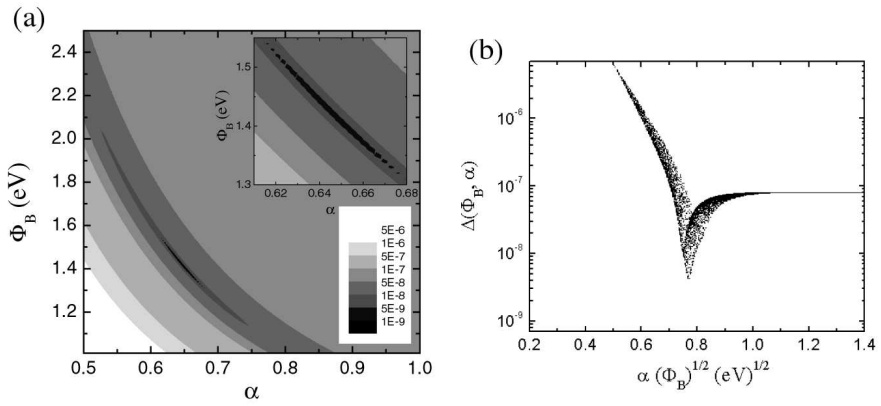

Fig. 6. (a) Contour plot of $\Delta(\Phi_B, \alpha)$ values for C12 nanopore device as a function of Φ_B and α, where the darker region corresponds to a better fitting. Inset shows detail minimization fitting regions. (b) A plot of $\Delta(\Phi_B, \alpha)$ as a function of a $\alpha\Phi_B^{1/2}$

adding an Au-thiol bonding length to the length of molecule [21]). Note that these lengths assume through-bond tunneling [21],[22],[31],[55]. The high and low bias regimes are defined somewhat arbitrarily by comparing the relative magnitudes of the first and second exponential terms in (2). Using $\Phi_B = 1.42$ eV and $\alpha = 0.65$ obtained from nonlinear least squares fitting of the C12 I(V) data, the second term becomes less than $\sim 10\%$ of the first term at ~ 0.5 Volt that is chosen as the boundary of low and high bias ranges.

As seen in Fig. 7, the tunneling current shows exponential dependence on molecular length, which is consistent with the Simmons tunneling model [see (3) and (4)]. The β values can be determined from the slope at each bias and are plotted in Fig. 8. The error bar of an individual β value in this plot was obtained by considering both the device size uncertainties and the linear fitting errors.

The determined β values are almost independent of bias in the low bias range ($V <\sim 0.5$ V), and an average β of 0.77 ± 0.06 Å^{-1} in this region (from 0 to 0.5 V) can be calculated from Fig. 8. The β value (0.77 ± 0.06 Å$^{-1} \approx 0.96 \pm 0.08$ per methylene) for alkanethiols reported here is comparable to previously reported values as summarized in Table 2. This β value agrees with the value of 0.79 Å^{-1}(β_0) calculated via (5) from fitting individual I(V) characteristic of the C12 device. The calculated β_0 of C8 and C16 devices also have similar values, as summarized in Table 3.

According to (6), β_V^2 depends on bias V linearly in the high bias range. The inset in Fig. 8 is a plot of β_V^2 versus V in this range (0.5 to 1.0 Volt) along with linear fitting of the data. From this fitting, $\Phi_B = 1.35 \pm 0.20$ eV and $\alpha = 0.66 \pm 0.04$ were obtained from the intercept and the slope, respectively, consistent with the values $\{\Phi_B = 1.42$ eV and $\alpha = 0.65\}$ obtained from the

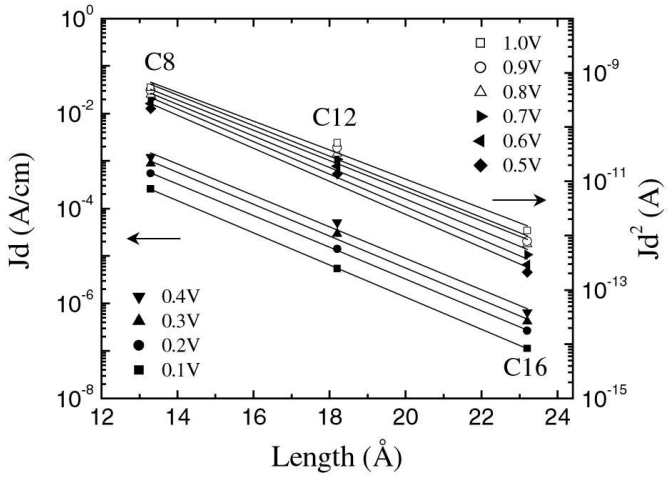

Fig. 7. Log plot of tunneling current densities multiplied by molecular length d at low bias and by d^2 at high bias (symbols) versus molecular lengths. The lines through the data points are linear fittings

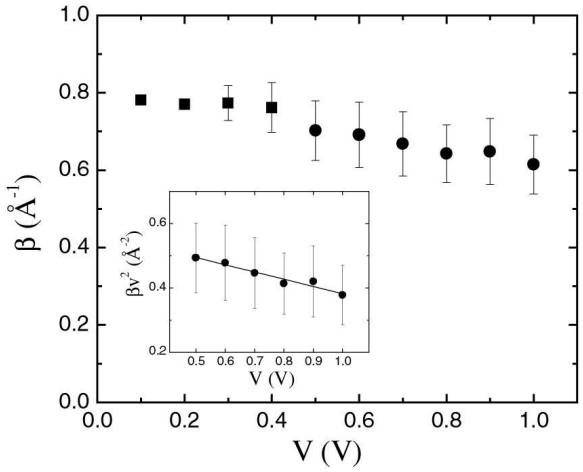

Fig. 8. Plot of β versus bias in the low bias range (square symbols) and high bias ranges (circular symbols). The inset shows a plot of β_V^2 versus bias with a linear fitting

Table 2. Summary of alkanethiol tunneling characteristic parameters

Junction	β ($Å^{-1}$)	J (A/cm^2) at 1 V	Φ_B (eV)	Technique	Ref.
(bilayer) monothiol	0.87 ± 0.1	25–200[a)]	2.1[e)]	Hg-junction	[24]
(bilayer) monothiol	0.71 ± 0.08	0.7–3.5[a)]		Hg-junction	[26]
monothiol	0.79 ± 0.01	1500 ± 200[b)]	1.4[e)]	Solid M-I-M	[32]
monothiol	1.2			STM	[18]
dithiol	0.8 ± 0.08	3.7–5×10^5 [c)]	5 ± 2[f)]	STM	[19]
monothiol	0.73–0.95	1100–1900[d)]	2.2[e)]	CAFM	[20]
monothiol	0.64–0.8	10-50[d)]	2.3[e)]	CAFM	[22]
dithiol	0.46 ± 0.02	3–6×10^5[c)]	1.3–1.5[e)]	CAFM	[23]
monothiol	1.37 ± 0.03		1.8[f)]	Tuning fork AFM	[47]
monothiol	0.97 ± 0.04			Electrochemical	[29]
monothiol	0.85			Electrochemical	[30]
monothiol	0.91 ± 0.08			Electrochemical	[31]
monothiol	0.76	2 ×10^4(at 0.1 V)	1.3–3.4[g)]	Theory	[56]
monothiol	0.76			Theory	[57]
monothiol	0.79			Theory	[54]

Note:
Some decay coefficients b were converted into the unit of $Å^{-1}$ from the unit of per methylene.
The junction areas were estimated by optical microscope[a)], SEM[b)], assuming single molecule[c)], and Hertzian contact theory[d)].
Current densities (J) for C12 monothiol or dithiol at 1 V are extrapolated from published results for other length molecules by using conductance $\propto \exp(-\beta\, d)$ relationship.
Barrier height Φ_B values were obtained from Simmons equation[e)], bias-dependence of β[f)], and a theoretical calculation[g)].

nonlinear least squares fitting in the previous section.

β values for alkanethiols obtained by various experimental techniques have previously been reported and are summarized in Table 2 [18]-[32],[47]. In order to compare with these reported β values, we also performed length-dependent analysis on our experimental data according to the generally used equation [19]-[27],[32]:

$$G = G_0 exp(-\beta d). \tag{7}$$

This gives a β value from 0.84 to 0.73 $Å^{-1}$ in the bias range from 0.1 to 1.0 volt, which is comparable to results reported previously. For example, Holmlin, et. al, reported a β value of 0.87 $Å^{-1}$ by mercury drop experiments [24], and Wold, et. al, have reported β of 0.94 $Å^{-1}$ and Cui, et. al, reported β of 0.64 $Å^{-1}$ for various alkanethiols by using a conducting atomic force microscope technique [20],[22]. These reported β were treated as bias-independent quantities, contrary to the results reported here and that observed in a

slightly different alkane system (ligand-encapsulated nanoparticle/alkanedithiol molecules) [23]. We also caution again the use of parameters that have not been checked against a temperature-dependent analysis, since small non-tunneling components can dramatically affect derived values of β.

Table 3. Summary of alkanethiol tunneling parameters in this study

Molecules	J (A/cm^2) at 1 V	Φ_B (eV)	α	m* (m)	β_0 (Å^{-1})*
C8	31,000 ± 10,000	1.83 ± 0.10	0.61 ± 0.01	0.37	0.85 ± 0.04
C12	1,500 ± 200	1.42 ± 0.04	0.65 ± 0.01	0.42	0.79 ± 0.02
C16	23 ± 2	1.40 ± 0.03	0.68 ± 0.01	0.46	0.82 ± 0.02
C8-dithiol	93,000 ± 18,000	1.20 ± 0.03	0.59 ± 0.01	0.35	0.66 ± 0.02

* β_0 values were calculated from (5) using Φ_B and α.

Franz Model

We have analyzed our experimental data using a Franz two-band model [48]-[51]. Since there is no reliable experimental data on the Fermi level alignment in these metal-SAM-metal systems, Φ_B and m* are treated as adjustable parameters. We performed a least squares fit on our data with the Franz non-parabolic E(k) relationship [see (1)] using an alkanethiol HOMO-LUMO gap of 8 eV[1]. Figure 9 shows the resultant E(k) relationship and the corresponding energy band diagrams. The zero of energy in this plot was chosen as the LUMO energy. The best fitting parameters obtained by minimizing χ^2 were $\Phi_B = 1.49 \pm 0.51$ eV and m* $= 0.43 \pm 0.15$ m, where the error ranges of Φ_B and m* are dominated by the error fluctuations of β [$-k^2 = (\beta/2)^2$]. Both electron tunneling near the LUMO and hole tunneling near the HOMO can be described by these parameters. $\Phi_B = 1.49$ eV indicates that the Fermi level is aligned close to one energy level in either case, therefore the Simmons model is a valid approximation. The Φ_B and m* values obtained here are in reasonable agreement with the previous results obtained from the Simmons model.

[1] Although the HOMO-LUMO gap of alkyl chain type molecules has been reported (see [12]), there is no experimental data on the HOMO-LUMO gap for Au/alkanethiol SAM/Au system. 8 eV is commonly used as HOMO-LUMO gap of alkanethiol

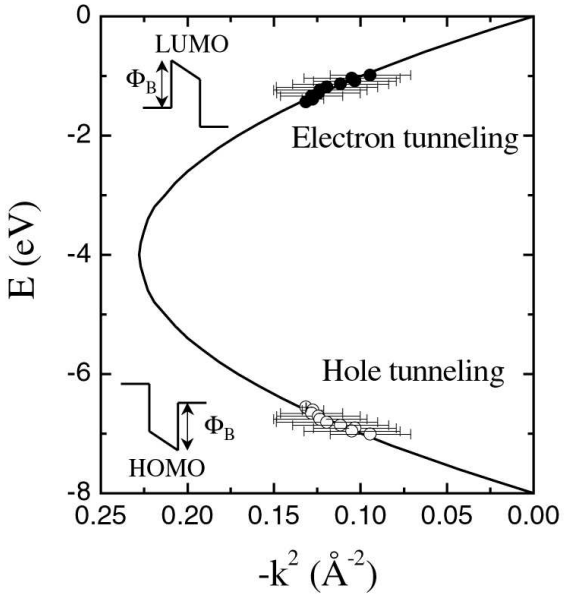

Fig. 9. E(k) relationship (symbols) generated from the length-dependent measurement data for alkanethiols. Solid and open symbols correspond to electron and hole, respectively. The insets show the corresponding energy band diagrams. The solid curve is the Franz two-band expression for m* = 0.43 m

4.2 Inelastic Tunneling

Inelastic Electron Tunneling Spectroscopy

Electronic transport through alkanethiol SAMs is further investigated with the technique of inelastic electron tunneling spectroscopy [33], such as the works of 1966 by Jaklevic and Lambe who studied the conductance of a tunnel junctions with encased organic molecules [34]. Since then it has become a powerful spectroscopic tool for chemical identification, chemical bonding investigation, and surface chemistry and physics studies [37]. In an inelastic tunneling process the electron loses energy to a localized vibrational mode with a frequency when the applied bias satisfies the condition of $eV = h\nu$ As a result, an additional tunneling channel is opened for the electron, resulting in an increase in the total current at the applied bias corresponding to the vibrational mode energy [36]. Typically only a small fraction of tunneling electrons are involved in the inelastic tunneling process (determined by the electron - vibronic mode coupling coefficient), resulting in a small conductance change, which is commonly measured in the second harmonics of a phase-sensitive detector that yields the characteristic frequencies of the corresponding vibrational modes as well as other information [35]-[37].

I(V,T) measurements and additional IETS studies have been performed on an octanedithiol (C8-dithiol) SAM using the aforementioned device structure shown in Fig. 1(a) [33]. Figure 10(a) is the I(V,T) data for this device obtained from 300 to 4.2 K. An Arrhenius plot shown in Fig. 10(b) exhibits little temperature dependence, verifying that tunneling is the main transport mechanism for C8-dithiol SAM. This result is in good agreement with the tunneling transport characteristics observed previously. Figure 11 shows the room temperature I(V) measurement result. Using a junction area of 51 ± 5 nm in diameter (obtained from statistical studies of the nanopore size with SEM), a current density of (9.3 ± 1.8) × 10^4 A/cm^2 at 1.0 Volt is calculated. As a comparison, the current density of (3.1 ± 1.0) × 10^4 A/cm^2 at 1.0 Volt was observed for C8 monothiol SAM. Using the modified Simmons model [see (2)], the transport parameters of Φ_B = 1.20 ± 0.03 eV and α = 0.59 ± 0.01 (m* = 0.34 m) were obtained for this C8-dithiol SAM.

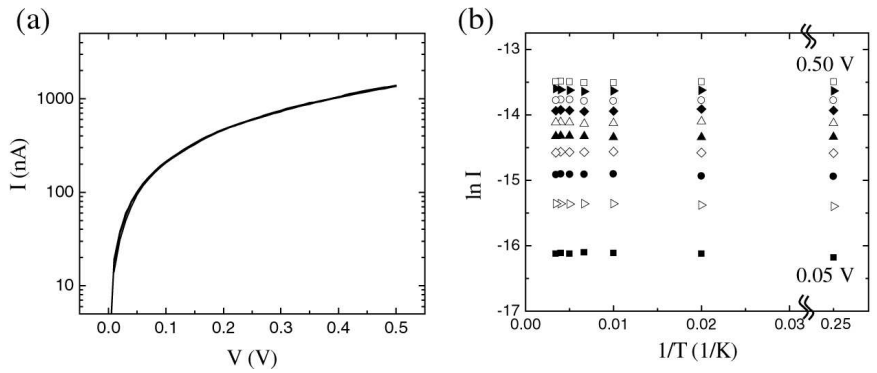

Fig. 10. (a) I(V,T) characteristics of C8-dithiol SAM at selected temperatures (4.2, 50, 100, 150, 200, 250, and 290 K). (b) Arrhenius plot generated from the data in (a), at voltages from 0.1 to 0.5 Volt with 0.05 Volt steps

Figure 12 shows the IETS spectrum of the same C8-dithiol SAM device obtained at T = 4.2 K. An ac modulation of 8.70 mV (rms value) at a frequency of 503 Hz was applied to the sample to acquire the second harmonic signals. The spectra are stable and repeatable upon successive bias sweeps. The spectrum at 4.2 K is characterized by three pronounced peaks in the 0 to 200 mV region at 33, 133, and 158 mV. From comparison with previously reported infrared (IR), Raman, and high resolution electron energy loss (HREEL) spectra of SAM covered gold surfaces (Table 4), these three peaks are assigned to ν(Au-S), ν(C-C), and $\gamma_w(CH_2)$ modes of a surface bound

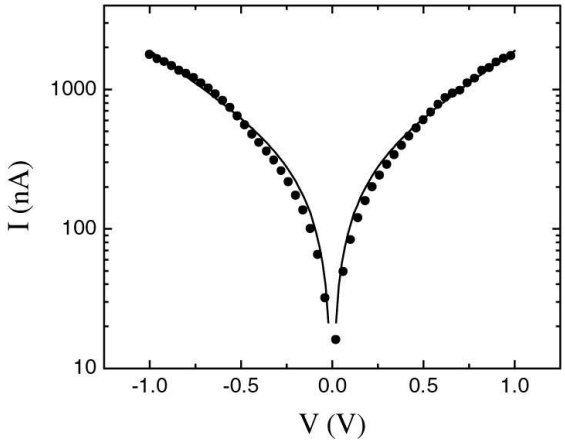

Fig. 11. Measured C8-dithiol I(V) data (circular symbols) is compared with calculation (solid curve) using the optimum fitting parameters of $\Phi_B = 1.20$ eV and $\alpha = 0.59$

alkanethiolate[2] [58]-[60]. The absence of a strong ν(S-H) signal at $\sim$ 329 mV suggests that most of the thiol groups have reacted with the gold bottom and top contacts. Peaks are also reproducibly observed at 80, 107, and 186 mV. They correspond to ν(C-S), $\delta_r(CH_2)$, and $\delta_s(CH_2)$ modes. The stretching mode of the CH_2 groups, $\nu(CH_2)$, appears as a shoulder at 357 meV. The peak at 15 mV is due to vibrations from either Si, Au, or δ(C-C-C) [61]. We note that all alkanethiolate peaks without exception or omission occur in the spectra. Peaks at 58, 257, 277, and 302, as well as above 375 mV are likely to originate from Si-H and N-H vibrations related to the silicon nitride membrane [61],[62], which forms the SAM encasement. Measurement of the background spectrum of an "empty" nanopore device with only gold contacts to obtain background contributions from Si_3N_4 is hampered by either too low (open circuit) or too high (short circuit) currents in such a device. However, to the best of our knowledge alkanethiols have no vibrational signatures in these regions. Similar IETS result has also been obtained using a different test structure recently [63].

Although there are no selection rules in IETS as there are in IR and Raman spectroscopy, certain selection preferences have been established. According to the IETS theory [64], molecular vibrations with net dipole moments perpendicular to the interface of the tunneling junction have larger peak intensities than vibrations with net dipole moments parallel to the interface (for dipoles close to the electrodes). Thus vibrations perpendicular to the electrode interface, i.e., ν(Au-S), ν(C-S), ν(C-C), and $\gamma_w(CH_2)$ dominate

[2]The symbols δ, γ, and ν denote in-plane rocking (r) and scissoring (s), out-of-plane wagging (w) and twisting (t), and stretching modes, respectively

the IETS spectrum while modes parallel to the interface, i.e., $\delta_{r,s}(CH_2)$ and $\nu(CH_2)$, are weak, as clearly shown in Fig. 12.

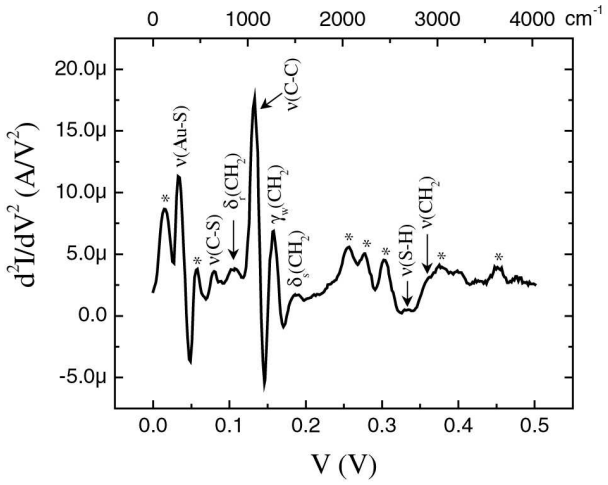

Fig. 12. Inelastic electron tunneling spectra of C8-dithiol SAM obtained from lock-in second harmonic measurements with an ac modulation of 8.70 mV (rms value) at a frequency of 503 Hz (T = 4.2 K). Peaks labeled * are most probably background due to the encasing Si_3N_4

Linewidth Study

In order to verify that the observed spectra are indeed valid IETS data, the peak width broadening was examined as a function of temperature and modulation voltage. IETS was performed with different ac modulations at a fixed temperature, and at different temperatures with a fixed ac modulation. Figure 13(a) shows the modulation dependence of the IETS spectra obtained at 4.2 K, and Fig. 13(b) shows the modulation broadening of the C-C stretching mode at 133 meV. The circular symbols are the full widths at half maximum (FWHMs) of the experimental peak at T = 4.2 K with various modulation voltages. A Gaussian distribution function was utilized to obtain a FWHM and the error range [65]. The square symbols are calculated FWHM values ($W_{theoretical}$) taking into account both a finite temperature effect ($W_{thermal} \sim 5.4\ k_BT$) and a finite voltage modulation effect ($W_{modulation} \sim 1.7\ Vac_{rms}$) [66]. These two broadening contributions add as the squares: $W^2_{theoretical} = W^2_{thermal} + W^2_{modulation}$. The agreement is excellent over most of the modulation range, but we note a saturation of the linewidth at low modulation bias indicating the influence of a non-negligible intrinsic linewidth. Taking into account the known thermal and modulation

Table 4. Summary* of the major vibrational modes of alkanethiolates. Taken from [58]-[60]

Modes	Methods	Wavenumber (cm^{-1})	(meV)
ν(Au-S)	HREELS	225	28
ν(Au-S)	Raman	641	79
	Raman	706	88
	HREELS	715	89
$\delta_r(CH_2)$	IR	720	89
	IR	766	95
	IR	925	115
	HREELS	1050	130
ν(C-C)	Raman	1064	132
	Raman	1120	139
	IR	1230	152
$\gamma_{w,t}(CH_2)$	HREELS	1265	157
	IR	1283	159
	IR	1330	165
$\delta_s(CH_2)$	HREELS	1455	180
ν(S-H)	Raman	2575	319
$\nu_s(CH_2)$	Raman	2854	354
	HREELS	2860	355
	Raman	2880	357
$\nu_{as}(CH_2)$	Raman	2907	360
	HREELS	2925	363

* There is a vast amount of literature with spectroscopic assignments for alkanethiols. The references given are representative for IR [60], Raman [58], and HREELS [59] assignments.

broadenings, and including the intrinsic linewidth (W_I) [67] broadening as a fitting parameter, the measured peak width (W_{exp}) is given by

$$W_{exp} = \sqrt{W_I^2 + W_{thermal}^2 + W_{modulation}^2} \tag{8}$$

W_I can be determined by using a nonlinear least squares fit to the ac modulation data (Fig. 13) with (8), giving an intrinsic linewidth of 3.73 ± 0.98 meV for this line. This is shown (with the error range) in Fig. 13(b) as a shaded bar, including the thermal contribution.

We can independently check the thermal broadening of the line at fixed modulation width. Figure 14 shows the temperature dependence of the IETS spectra obtained with an ac modulation of 8.70 mV (rms value). In Fig. 14(b) the circular symbols (and corresponding error bars) are experimental FWHM values of the C-C stretching mode from Fig. 14(a), determined by a Gaus-

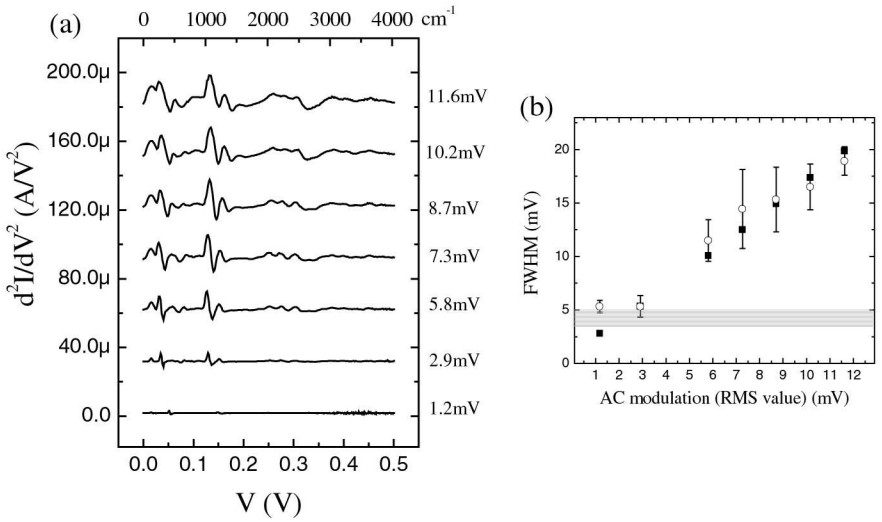

Fig. 13. (a) Modulation dependence of IETS spectra obtained at 4.2 K. (b) Line (C-C stretching mode) broadening as a function of ac modulation. The circular symbols are experimental FWHMs and the square symbols are theoretical calculations considering both modulation and thermal contributions. The shaded bar denotes the expected saturation due to the derived intrinsic linewidth (including a 5.4 k_BT thermal contribution) of 3.73 ± 0.98 meV

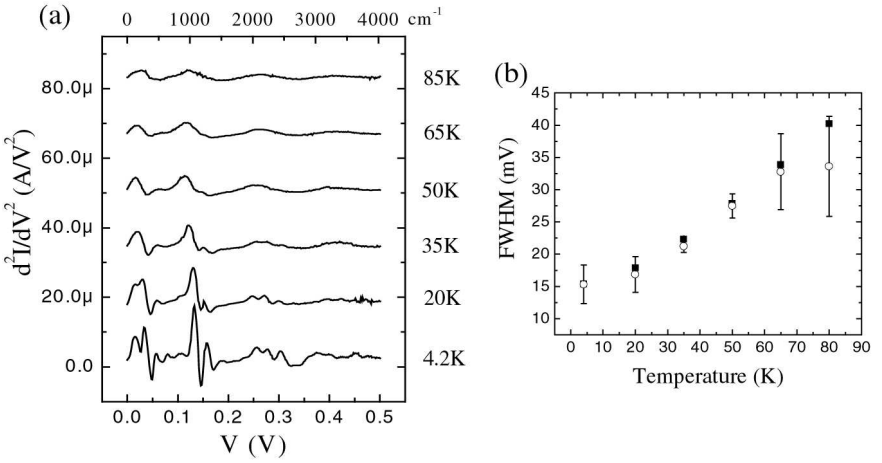

Fig. 14. (a) Temperature dependence of IETS spectra obtained at a fixed ac modulation of 8.70 mV (rms value). (b) Line (C-C stretching mode) broadening as a function of temperature. The circular symbols are experimental FWHMs and the square symbols are theoretical calculations considering thermal broadening, modulation broadening, and the intrinsic linewidth

sian fit (and error of the fit) to the experimental lineshape. For simplicity we have only considered Gaussian lineshapes [65] resulting in increased error bars for the lower temperature range due to an asymmetric lineshape. The square symbols are theoretical calculations considering thermal broadening, modulation broadening, and the intrinsic linewidth determined above. The error ranges of the calculation (due to the intrinsic linewidth error) are approximately the size of the data points. The agreement between theory and experiment is very good, spanning a temperature range from below ($\times$ 0.5) to above ($\times$ 10) the thermally broadened intrinsic linewidth. This linewidth should be a sensitive test to compare to theoretical models of transmission probabilities [68].

Similar intrinsic linewidths have been determined for the Au-S stretching mode (33 meV) and CH_2 wagging mode (158 meV), and the results are shown in Fig. 15. For the Au-S stretching mode, the deviation of experimental data from calculated values is little, indicating that its intrinsic linewidth is small. A linewidth upper limit of 1.69 meV is determined for this vibrational mode. For the CH_2 wagging mode, nonlinear least squares fit to (8) [the solid curve in Fig. 15(b)] gave intrinsic linewidth of 13.5 $\pm$ 2.4 meV. The linewidths and their variation throughout the molecule are potentially due to inhomogeneous line broadening, and a more detailed understanding may give detailed structural information of these device structures.

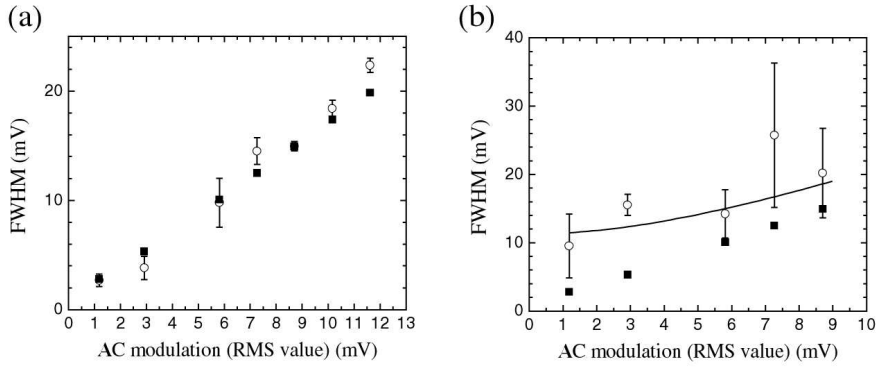

Fig. 15. Line broadenings as function of ac modulation for IETS spectra obtained at 4.2 K for (a) the Au-S stretching mode and (b) the CH_2 wagging mode. The circular symbols are experimental FWHMs and the square symbols are theoretical calculations considering both modulation and thermal contributions (but not intrinsic linewidth). Nonlinear least squares fitting to (8) to determine intrinsic linewidth is shown as the solid curve in (b)

5 Conclusions

We present here a study of electron tunneling through alkanethiol SAMs, with the intent that this system can serve as a simple control for the development of well-characterized molecular junctions. The characteristics are consistent with accepted models of M-I-M tunneling junctions, as well as presenting a system on which tunneling spectroscopy can be performed.

The field of "molecular electronics" is rich in the proposal and promise of numerous device concepts [69],[70] but unfortunately has an absence of reliable data and characterization techniques upon which to test these ideas. It is incumbent upon the experimentalist to carefully institute controls to carefully validate claims of intrinsic molecular behavior. Systematic controls, such as the model system presented here, should assist in guiding further work toward a rational development of the fascinating device structures and systems that the field promises.

Acknowledgements

The authors would like to thank J. F. Klemic, X. Li, and R. Munden for helpful discussions and assistance. We especially thank I. Kretzschmar for assistance in identification of the IETS spectra. This work was supported by DARPA/ONR (N00014-01-1-0657), ARO (DAAD19-01-1-0592), AFOSR (F49620-01-1-0358), NSF (DMR-0095215), and NASA (NCC 2-1363). The fabrication was performed in part at the Cornell Nano-Scale Science & Technology Facility.

References

1. M.A. Reed, J.M. Tour, Scientific American 2000, June pp 86–93
2. M.A. Reed, C. Zhou, C.J. Muller et al: Science **278**, 252 (1997)
3. M.A. Reed, T. Lee, eds. *Molecular Nanoelectronics* (American Scientific Publishers, Stevenson Ranch 2003)
4. J.R. Heath, M.A. Ratner: Physics Today 2003, May pp 43–49; A. Nitzan, M.A. Ratner: Science **300** 1384 (2003)
5. Y. Chen, G.-Y. Jung, D.A. Ohlberg et al: Nanotechnology **14** 462 (2003); Beyond Silicon: Breakthroughs in Molecular Electronics, http://www.hpl.hp.com/research/qsr/ (Hewlett-Packard Quantum Science Research)
6. Y. Luo, C.P. Collier, J.O. Jeppesen et al: Chem. Phys. Chem. **3** 519 (2002); C.P. Collier, G. Mattersteig, E.W. Wong et al: Science **289** 1172 (2000)
7. D.R. Stewart, D.A.A. Ohlberg, P.A. Beck et al: Nano Lett. **4** 133 (2004); C.N. Lau, D.R. Stewart, R.S. Williams et al: Nano Lett. **4** 569 (2004)
8. T. Lee, W. Wang, J.F. Klemic et al: J. Phys. Chem. B in press (2004).
9. A. Ulman: *An Introduction to Ultrathin Organic Films from Langmuir-Blodgett to Self-Assembly* (Academic Press, Boston 1991)

10. G.E. Poirier: Chem. Rev. **97** 1117 (1997)
11. M.A. Ratner, B. Davis, M. Kemp et al: In *Molecular Electronics: Science and Technology*, The Annals of the New York Academy of Sciences, vol 852, ed by A. Aviram, M.A. Ratner (The New York Academy of Sciences, New York 1998)
12. C. Boulas, J.V. Davidovits, F. Rondelez et al: Phys. Rev. Lett. **76** 4797 (1996); M. Fujihira, H. Inokuchi: Chem. Phys. Lett. **17** 554 (1972); S.G. Lias, J.E. Bartmess, J.F. Liebman et al: *Gas-Phase Ion and Neutral Thermochemistry*, J. Phys. Chem. Ref. Data, **17**(1) 24 (1998)
13. M.W. Walczak, C. Chung, S.M. Stole et al: J. Am. Chem. Soc. **113** 2370 (1991)
14. R.G. Nuzzo, B.R. Zegarski, L.H. Dubois: J. Am. Chem. Soc. **109** 733 (1987)
15. C.A. Widrig, C. Chung, M.D. Porter: J. Electroanal. Chem. **310** 335 (1991)
16. G.E. Poirier, M.J. Tarlov: Langmuir **10** 2853 (1994)
17. M.D. Porter, T.B. Bright, D.L. Allara et al: J. Am. Chem. Soc. **109** 3559 (1987)
18. L.A. Bumm, J.J. Arnold, T.D. Dunbar et al: J. Phys. Chem. B **103** 8122 (1999)
19. B. Xu, N.J. Tao: Science **301** 1221 (2003)
20. D.J. Wold, C.D. Frisbie: J. Am. Chem. Soc. **123** 5549 (2001)
21. D.J. Wold, R. Haag, M.A. Rampi et al: J. Phys. Chem. B **106** 2813 (2002)
22. X.D. Cui, X. Zarate, J. Tomfohr et al: Nanotechnology **13** 5 (2002)
23. X.D. Cui, A. Primak, X. Zarate et al: J. Phys. Chem. B **106** 8609 (2002)
24. R. Holmlin, R. Haag, M.L. Chabinyc et al: J. Am. Chem. Soc. **123** 5075 (2001)
25. M.A. Rampi, G.M. Whitesides: Chem. Phys. **281** 373 (2002)
26. K. Slowinski, H.K.Y. Fong, M. Majda: J. Am. Chem. Soc. **121** 7257 (1999)
27. R.L. York, P.T. Nguyen, K. Slowinski: J. Am. Chem. Soc. **125** 5948 (2003)
28. J.G. Kushmerick, D.B. Holt, S.K. Pollack et al: J. Am. Chem. Soc. **124** 10654 (2002)
29. J.F. Smalley, S.W. Feldberg, C.E.D. Chidsey et al: J. Phys. Chem. **99** 13141 (1995)
30. K. Weber, L. Hockett, S. Creager: J. Phys. Chem. B **101** 8286 (1997)
31. K. Slowinski, R.V. Chamberlain, C.J. Miller et al: J. Am. Chem. Soc. **119** 11910 (1997)
32. W. Wang, T. Lee, M.A. Reed: Phys. Rev. B **68** 035416 (2003)
33. W. Wang, T. Lee, I. Kretzschmar et al: Nano Lett. **4** 643 (2004)
34. R.C. Jaklevic, J. Lambe: Phys. Rev. Lett. **17** 1139 (1966)
35. J. Lambe, R.C. Jaklevic: Phys. Rev. **165** 821 (1968)
36. C.J. Adkins, W.A. Phillips: J. Phys. C: Solid State Phys. **18** 1313 (1985)
37. P.K. Hansma, Ed. *Tunneling Spectroscopy: Capabilities, Applications, and New Techniques* (Plenum, New York 1982)
38. B.C. Stipe, M.A. Rezaei, W. Ho: Science **280** 1732 (1998)
39. C. Zhou, M.R. Deshpande, M.A. Reed et al: Appl. Phys. Lett. **71** 611 (1997)
40. J. Chen, M.A. Reed, A.M. Rawlett et al: Science **286** 1550 (1999); J. Chen, L.C. Calvet, M.A. Reed et al: Chem. Phys. Lett. **313** 741 (1999)
41. K.S. Ralls, R.A. Buhrman, R.C. Tiberio: Appl. Phys. Lett. **55** 2459 (1989)
42. R.M. Metzger, B. Chen, U. Ho1pfner et al: J. Am. Chem. Soc. **119** 10455 (1997)
43. P. Horowitz, W. Hill: *The Art of Electronics*, (Cambridge University Press, New York 1989)
44. S.M. Sze: *Physics of Semiconductor Devices* (Wiley, New York 1981)
45. R.E. Thurstans, D.P. Oxley: J. Phys. D: Appl. Phys. **35** 802 (2002); J.C. Simmons, R.R. Verderber: Prof. Roy. Soc. A. **301** 77 (1967); G. Dearnaley, A.M. Stoneham, D.V. Morgan: Rep. Prog. Phys. **33** 1129 (1970)

46. B. Mann, H.J. Kuhn: J. Appl. Phys. **42** 4398 (1971); E.E. Polymeropoulos, J. Sagiv: J. Chem. Phys. **69** 1836 (1978)
47. F.F. Fan, J. Yang, L. Cai et al: J. Am. Chem. Soc. **124** 5550 (2002)
48. W. Franz: In *Handbuch der Physik*, vol 17, ed by S. Flugge (Springer-Verlag, Berlin 1956)
49. G. Lewicki, C.A. Mead: Phys. Rev. Lett. **16** 939 (1966); R. Stratton, G. Lewicki, C.A. Mead: J. Phys. Chem. Solids. **27** 1599 (1966); G.H. Parker, C.A. Mead: Phys. Rev. Lett. **21** 605 (1968)
50. B. Brar, G.D. Wilk, A.C. Seabaugh: Appl. Phys. Lett. **69** 2728 (1996)
51. C. Joachim, M. Magoga: Chem. Phys. **281** 347 (2002)
52. J.G. Simmons: J. Appl. Phys. **34** 1793 (1963)
53. J.G. Simmons: J. Phys. D **4** 613 (1971); J. Maserjian, G.P. Petersson: Appl. Phys. Lett. **25** 50 (1974)
54. Tomfohr, J. K.; Sankey, O. F. Phys. Rev. B 2002, 65, 245105.
55. H. Yamamoto, D.H. Waldeck: J. Phys. Chem. B **106** 7469 (2002); A.M. Napper, H. Liu, D.H. Waldeck: J. Phys. Chem. B **105** 7699 (2001)
56. C.-C. Kaun, H. Guo: Nano Lett. **3** 1521 (2003)
57. S. Piccinin, A. Selloni, S. Scandolo et al: J. Chem. Phys. **119** 6729 (2003)
58. M.A. Bryant, J.E. Pemberton: J. Am. Chem. Soc. **113** 8284 (1991)
59. H.S. Kato, J. Noh, M. Hara et al: J. Phys. Chem. B **106** 9655 (2002)
60. C. Castiglioni, M. Gussoni, G. Zerbi: J. Chem. Phys. **95** 7144 (1991)
61. M. Molinary, H. Rinnert, M. Vergnat et al: Mat. Sci. Eng. B **69** 301 (2003); P.D. Bogdanoff, B. Fultz, S. Rosenkranz: Phys. Rev. B **60** 3976 (1999); U. Mazur, K.W. Hipps: J. Phys. Chem. **86** 2854 (1982)
62. U. Mazur, K.W. Hipps: J. Phys. Chem. **85** 2244 (1981);H. Kurata, M. Hirose, Y. Osaka: Jap. J. Appl. Phys. **20** L811 (1981)
63. J.G. Kushmerick, J. Lazorcik, C.H. Patterson et al: Nano Lett. **4** 639 (2004)
64. J. Kirtley, J.T. Hall: Phys. Rev. B **22** 848 (1980)
65. I.J. Lauhon, W. Ho: Phys. Rev. B **60** R8525 (1999)
66. J. Klein, A. Leger, M. Belin et al: Phys. Rev. B **7** 2336 (1973)
67. L.J. Lauhon, W. Ho: Rev. Sci. Instrum. **72** 216 (2001)
68. M.A. Kastner: Physics Today 1993, January pp 24–31
69. A. Aviram, M. Ratner, eds. *Molecular Electronics: Science and Technology*, The Annals of the New York Academy of Sciences, vol. 852 (The New York Academy of Sciences, New York 1998)
70. J. Reimers, C. Picconatto, J. Ellenbogen et al: *Molecular Electronics III*, The Annals of the New York Academy of Sciences, vol. 1006 (The New York Academy of Sciences, New York 2003)